

# Electron induced molecular desorption from electron clouds at the Relativistic Heavy Ion Collider

Ubaldo Iriso\* and Wolfram Fischer†

Brookhaven National Laboratory, Upton, New York 11973, USA

(Received 2 July 2005; published 8 November 2005; corrected 9 November 2005)

Molecular desorption coefficients from electron bombardment of the warm Relativistic Heavy Ion Collider beam pipe are derived from measurements for both baked and unbaked stainless steel. For this, we analyze electron detector and pressure gauge signals in the presence of an electron cloud. Finally, we present a comparison between the measured and simulated energy spectrum of the cloud electrons.

DOI: [10.1103/PhysRevSTAB.8.113201](https://doi.org/10.1103/PhysRevSTAB.8.113201)

PACS numbers: 29.27.Bd, 68.47.-b, 07.30.Kf

## I. INTRODUCTION

The knowledge of molecular desorption coefficients is a key ingredient in understanding the electron cloud induced pressure rises, which are limiting machine operation in Relativistic Heavy Ion Collider (RHIC) since 2001 [1–4]. RHIC was not equipped with electron detectors when the first pressure rises occurred. During the 2002 RHIC shutdown, electron detectors (ED) were installed in the RHIC rings to allow better diagnostics in the subsequent runs. In the following, we analyze the experimental data taken with these electron detectors as well as vacuum gauges during 2003 for an unbaked surface, and 2004 for a baked surface.

Assuming the beam pipe is a periodic structure with vacuum pumps of pumping speed  $2S$  spaced by the distance  $2L$ , the pressure distribution along the longitudinal position  $z$  between two vacuum pumps is [5]:

$$P(z) = q \left[ \frac{2Lz - z^2}{2c} + \frac{L}{S} \right], \quad \text{for } 0 \leq z \leq 2L, \quad (1)$$

where the  $z$  origin is placed at one of the vacuum pumps,  $c$  is the specific molecular conductance of the vacuum chamber, and  $q$  is the specific linear outgassing rate. We only consider the outgassing rate due to an electron flux,  $dI/dl$ , in situations where it exceeds the thermal outgassing rate by a wide margin. In the absence of magnetic fields and assuming a regular and homogeneous chamber, we can further consider the electron flux to be constant throughout the beam pipe. The outgassing rate then does not depend on the longitudinal position  $z$ , and it can be expressed by

$$q = \eta_e \frac{kT}{e} \frac{dI}{dl}, \quad (2)$$

where  $e$  is the absolute value of the electron charge,  $k$  is Boltzmann's constant,  $T$  is the temperature, and  $\eta_e$  is the electron induced molecular desorption coefficient of the beam-pipe wall, that is, the number of desorbed molecules per impinging electron.

The electron flux  $dI/dl$  is not constant in time. Figure 1 shows a typical evolution of the electron flux during a RHIC turn in a simulation using CSEC [6,7]. The simulation is for a bunch train of 110 bunches with  $8 \times 10^{10}$  protons/bunch, and it illustrates the relevant features of an electron cloud buildup as a function of time. The result is numerically smoothed with a 10 MHz filter, which is also used in measurements with the electron detectors. As seen in the picture initially the electron flux grows exponentially, and it saturates after  $\approx 8 \mu\text{s}$  due to space charge effects [8]. During the abort gap, the electron flux decays rapidly. This behavior repeats at every turn. Since the time constant of the vacuum pumps is a few seconds [9], the pressure evolution cannot be followed within a turn. The pressure responds then to the flux, time averaged over one turn,

$$\left\langle \frac{dI}{dl} \right\rangle_\tau = \frac{1}{\tau} \int_0^\tau \frac{dI(t)}{dl} dt, \quad (3)$$

where  $\tau$  is the revolution period, and  $dI(t)/dl$  is the instantaneous electron flux. Using Eq. (3), the pressure due to an electron cloud at a given position of the beam pipe  $z$  is

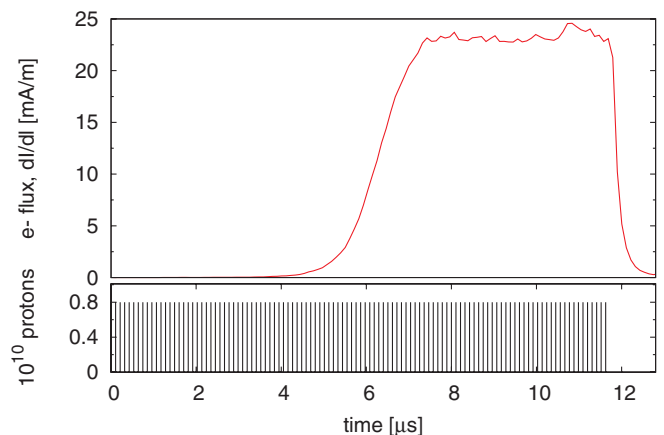


FIG. 1. (Color) The top plot shows a typical evolution of the electron flux during a revolution when RHIC is filled with a train of 110 bunches (bottom plot). This is a simulation using CSEC with an intensity of  $8 \times 10^{10}$  protons/bunch. The pressure is proportional to the time averaged electron flux in one turn, not to the peak value.

\*Electronic address: [ubaldo@bnl.gov](mailto:ubaldo@bnl.gov)

†Electronic address: [Wolfram.Fischer@bnl.gov](mailto:Wolfram.Fischer@bnl.gov)

TABLE I. Parameters used to estimate the electron desorption coefficient for the baked and unbaked surface.

Parameter	Symbol	Unit	Value unbaked location	Value baked location
Distance between pumps	$2L$	m	17	7
Pumping speed for CO	$2S$	l/s	140	270
Beam-pipe radius	$b$	cm		6
Line impedance	$Z$	$\Omega$		50
Amplifier gain	$G$	$\dots$		1600
Electron detector area	$A_{ED}$	$\text{cm}^2$		78
Effective transparency	$T_{\text{eff}}$	%		5

$$P(z) = P_0 + \eta_e \frac{kT}{e} \left\langle \frac{dI}{dl} \right\rangle_{\tau} \left[ \frac{2Lz - z^2}{2c} + \frac{L}{S} \right], \quad (4)$$

where  $P_0$  is the static pressure.

Equation (4) shows that, at a given location  $z$  the pressure is directly proportional to the electron desorption coefficient,  $\eta_e$ . This coefficient depends on the energy of the striking electron, the surface material, and the accumulated dose on the surface. For electrons below 100 eV, only a small amount of data exist in the literature. This is unfortunate, since the energy of the multipacting electrons for RHIC conditions falls within this range (as it is seen in Refs. [6,10] and Sec. V). For stainless steel, data for energies as low as 300 eV are found in Ref. [11], for OFHC Copper for energies as low as 20 eV in Ref. [12]. The desorption coefficient changes depending on the released gas as well. Since the experimental setup in RHIC does not have a residual gas analyzer to investigate the pressure composition, all calculations are done for CO at room temperature. Nevertheless, we point out that the gas

composition without beam in RHIC is mostly  $\text{H}_2$ , and CO increases faster (ratio wise) in presence of beam than  $\text{H}_2$  [9]. The pumping speed is obtained from the manufacturers' specifications (see Table I).

We first test whether Eq. (4) holds for the RHIC case. Then, from the analysis of the experimental data, the desorption coefficient and its evolution over weeks of operation is obtained. This analysis is done for two different locations, with two different surfaces, and during two different runs. The single beam vacuum chamber at "BO2" during 2003 was unbaked stainless steel. The common beam pipe at "IR12" during 2004 was baked stainless steel.

## II. EXPERIMENTAL SETUP

### A. The electron detector at the Relativistic Heavy Ion Collider

A sketch of the electron detector installed in RHIC is shown in Fig. 2. This detector is often called *retarding field*

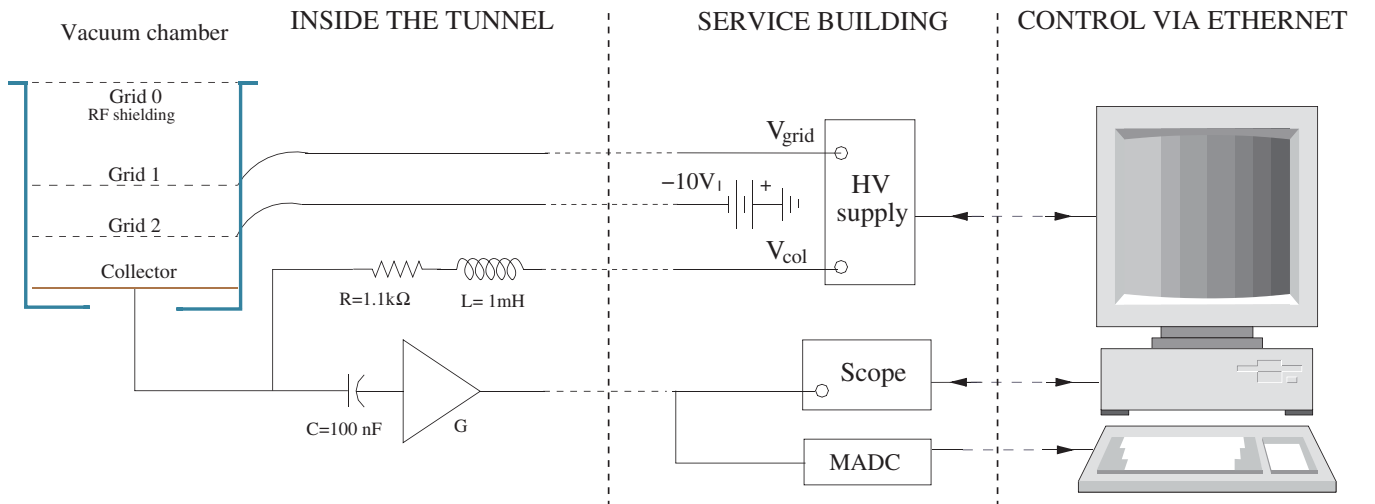


FIG. 2. (Color) RHIC electron detector layout. Part of the electron flux hitting the chamber wall reaches the collector plate. The signal is then magnified using the amplifier (marked with a  $G$ ) and transmitted to the scope. Grid 1 is used to filter the energy and bias the collector plate using the high voltage supply. The capacitor between the collector plate and the amplifier protects the latter device from dc current created by the bias voltage. The MADC (multiplex analog to digital converter) digitally reports the peak electron signals with a frequency of 1 Hz.

analyzer (RFA) because it is able to analyze the energy of the multipacting electrons by means of an electrostatic retarding field. The RHIC electron detector is based on the first PSR design [13], although similar detectors had also been installed in other machines, like APS [14], SPS [15], and BEPC [16]. In RHIC, the RFA is mounted on a 120 mm inner diameter tee, perpendicular to the vacuum pipe.

The top grid (“grid 0” in Fig. 2) is welded to the beam pipe and acts as an rf shield. Its transparency ( $T_0$ ) is fixed at 23% in order to decrease the effect of the image currents (see Ref. [17]) without interfering with the multipacting process. The middle grid (“grid 1” in Fig. 2, with  $T_1 = 80\%$ ) can be biased to different voltages ( $V_{\text{grid}}$ ), and acts as an electron energy filter: electrons with energy lower than  $|eV_{\text{grid}}|$  cannot traverse grid 1 and are not collected. This is why it is also called “filter grid.” The bottom grid (grid 2 in Fig. 2, with  $T_2 = 80\%$ ) is held at  $-10$  V by a dc battery as shown in Fig. 2. This was originally conceived to repel back the secondary electrons produced at the collector. However, after the installation of the electron detectors in the RHIC ring, a larger signal is observed when this grid is grounded. Thus, this grid is always grounded unless otherwise stated.

The collector can be biased either positively or negatively ( $V_{\text{col}}$  in Fig. 2) to check the presence of either electrons or ions (yet no ion signal has been detected so far). The signal produced by the electrons hitting the collector is finally carried to the data acquisition system. Typically, the scope takes a snapshot of the electron signal during one turn every 4 sec. The signal has a time resolution of 1 ns, and it is smoothed with a 10 MHz filter.

The multiplex analogical to digital converter, MADC, is used to obtain the peak electron signal with a sampling rate of 1 Hz. Because of the low sampling rate, this process has a large attenuation and it is used for applications where the relative values are important, not for absolute measurements [17].

For a given scope signal  $V$ , the flux into the wall per unit area is given by

$$\frac{dI}{dA} = \frac{V}{ZGA_{\text{ED}}T_{\text{eff}}}, \quad (5)$$

which accounts for the line impedance  $Z$ , the amplifier gain  $G$ , the area of the collector  $A_{\text{ED}}$ , and the effective transparency of the electron detector  $T_{\text{eff}}$ . The latter evaluates the electrons lost between the grids and the collector. In principle, assuming no electrons are lost when traversing the path between grid 0 and the collector (see Fig. 2) the effective transparency would be estimated as  $T_{\text{eff}} = T_0T_1T_2 \approx 15\%$ . However, this ideal relation does not take into account the electron energy: low energy electrons have a larger probability to be lost between the grids than high energy ones. The appendix shows that a good average value is  $T_{\text{eff}} = 5\%$ . In the following, the experimental data

are always quoted in [V]. Taking into account the values listed in Table I, for a given voltage the corresponding electron flux per unit area is obtained by

$$\frac{dI}{dA} \left[ \frac{\mu\text{A}}{\text{cm}^2} \right] \approx 3.2 \text{ V} \quad [\text{V}]. \quad (6)$$

Using the beam-pipe radius,  $b$ , the flux per unit length  $dI/dl$  is related to the flux per unit area  $dI/dA$  by

$$\frac{dI}{dl} = \frac{dI}{dA} 2\pi b. \quad (7)$$

Using Eqs. (5) and (7), we can express the electron flux time averaged over one turn  $\langle dI/dl \rangle_\tau$  by

$$\left\langle \frac{dI}{dl} \right\rangle_\tau = \frac{2\pi b}{ZGA_{\text{ED}}T_{\text{eff}}} \langle V \rangle_\tau, \quad (8)$$

where  $\langle V \rangle_\tau$  is the electron detector voltage time averaged over one turn,

$$\langle V \rangle_\tau = \frac{1}{\tau} \int_0^\tau V(t) dt, \quad (9)$$

which is measured using the equipment shown in Fig. 2. But the RHIC electron detectors described here are ac coupled to the system electronics. To calculate a nonzero average over one turn, we shift the baseline by the maximum value in the electron detector snapshot. The average over one revolution is then calculated by

$$\frac{1}{\tau} \int_0^\tau V(t) dt = \frac{1}{N} \sum_{i=1}^N [V_i - V_{\text{max}}], \quad (10)$$

where  $N$  is the number of samples in one revolution. Figure 3 depicts two examples of an electron detector

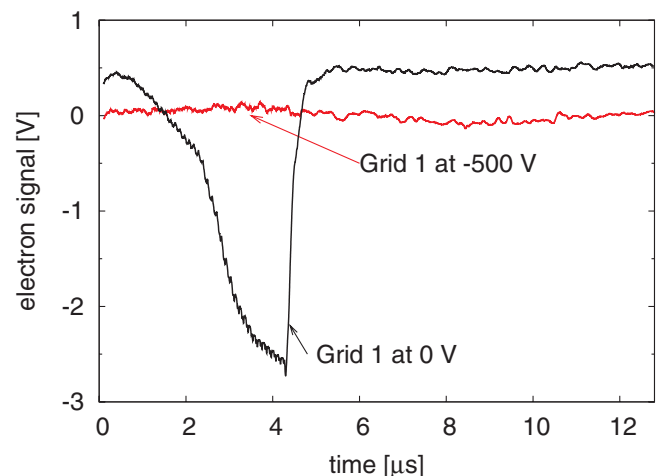


FIG. 3. (Color) Two electron detector snapshots of a RHIC revolution with 40 injected bunches spaced by 108 ns, and an average bunch intensity of  $N_b = 16 \times 10^{10}$  protons. Without voltage at grid 1 ( $V_{\text{grid}} = 0$  V), an electron multipacting signal is observed (black trace). The signal disappears when  $V_{\text{grid}} = -500$  V (red trace).

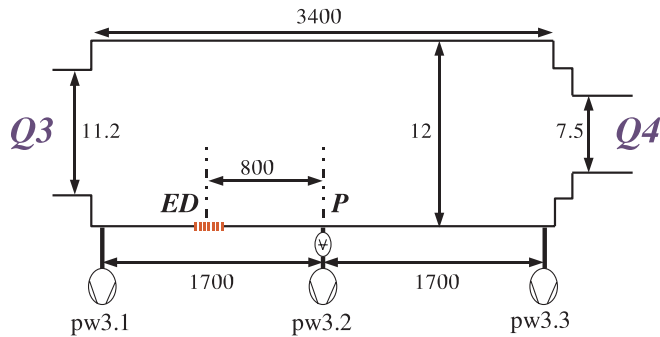


FIG. 4. (Color) Geometry of the single beam pipe BO2, made of stainless steel and unbaked during 2003. The electron detector location (marked with *ED*) is about 8 m away from the pressure gauge and ion pump, whose location is marked with *P*. Distances are given in cm and are not to scale.

snapshot during a RHIC revolution. The black trace corresponds to a snapshot with null grid 1 voltage, the red trace corresponds to a signal with  $V_{\text{grid}} = -500$  V. The buildup and decay of the multipacting signal is clear when  $V_{\text{grid}} = 0$  V, and it goes from positive (about 0.5 V) to negative values (about  $-2.5$  V) due to the ac coupling (a dc coupled signal would be only negative due to the negative sign of the electrons). By applying a  $V_{\text{grid}} = -500$  V, the signal disappears (red trace) and it shows that the multipacting electrons have an energy below 500 eV.

### B. Unbaked surface instrumentation

During 2003, approximately 60% of the warm RHIC beam pipes were baked. Beam injection is inhibited when the pressure at any location in the ring reaches an unacceptable level. These limits were approached within the 40% of the unbaked regions, where the electron multipacting thresholds are lower than in the baked regions. The pressure rises in unbaked regions prevented that multipacting conditions in baked regions were reached. In this situation, the only electron detector in an unbaked region (labeled as BO2) is easily exposed to electron clouds, and only few electron clouds were detected in the baked regions. Therefore, the analysis during 2003 uses the instrumentation in the unbaked single beam pipe shown in Fig. 4, which we treat as the periodic structure mentioned in Sec. I. The vacuum pump and pressure gauge are at the same location, the electron detector is 8 m away. Since the beam pipe between the ED and the vacuum pump/gauge is made of the same material, we can assume that the electron flux is the same throughout the entire region. In this situation, we can correlate the pressure at the gauge “pw3.2” ( $z = 0$ ) with the electron detector signal using Eq. (4),

$$P(z = 0) = P_0 + \eta_e \frac{kT}{e} \left\langle \frac{dI}{dl} \right\rangle_{\tau} \frac{L}{S}. \quad (11)$$

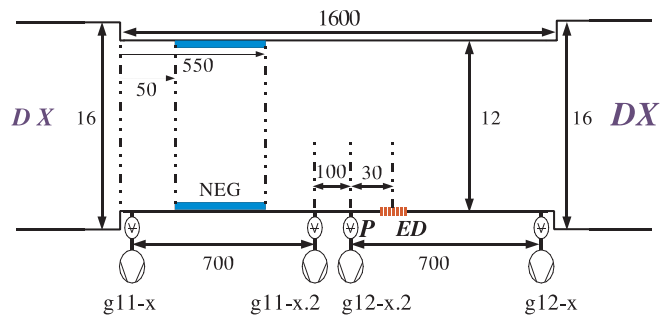


FIG. 5. (Color) Geometry of the common beam pipe IR12, made of baked stainless steel. The electron detector location (marked with *ED*) is only 0.3 m away from the pressure gauge and vacuum ion pump, whose location is marked with *P*. Distances are given in cm and are not to scale.

The same result is found if we place the origin ( $z = 0$ ) at pw3.1 because of the symmetric properties of Eq. (1).

Using Eqs. (8) and (11), we can express the pressure as a function of the electron detector voltage by

$$P = P_0 + \eta_e \frac{kT}{e} \frac{L}{S} \frac{2\pi b}{ZGA_{\text{ED}} T_{\text{eff}}} \langle V \rangle_{\tau}. \quad (12)$$

### C. Baked surface instrumentation

Approximately 80% of the warm beam pipes in RHIC were baked by 2004, including the aforementioned section BO2. During the polarized proton run, electron clouds were often detected in the common beam pipe, labeled as IR12. Two beams in opposite directions traversing a common beam pipe produce either larger bunch intensities than in the single beam pipes, or shorter bunch spacings than the ones in the single beam pipes. Therefore, electron cloud thresholds in the common beam-pipe regions are easier to reach, and the analysis is performed using the instrumentation in the common (and baked) beam pipe shown in Fig. 5. The electron detector, vacuum pump, and pressure gauges are only 0.3 m apart. We assume all this instrumentation is at the same location, and use Eq. (4) for  $z = 0$ . Thus, the calculation of the pressure as a function of the voltage in the ED follows again Eq. (12) using the values for baked surfaces in Table I.

## III. ELECTRON INDUCED DESORPTION OF UNBAKED STAINLESS STEEL

Figure 6 shows an example of experimental data. The top plot shows the time evolution of the pressure at the gauge pw3.2 (red line, right vertical axis), and the electron signal averaged over one turn [black dots, left vertical axis, calculated using Eq. (9)] as beam is injected (bottom plot). At about 16h17m30s, the injection is interrupted and the beam is dumped due to the large pressure in the rf cavities.

A linear relation between the pressure readings and the electron signal averaged over one turn is confirmed in

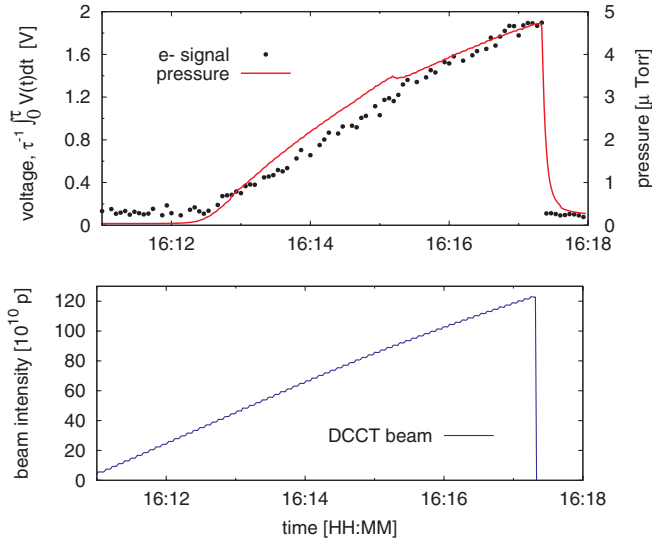


FIG. 6. (Color) Pressure and electron signal evolution (top plot), as the blue beam is being injected (bottom plot). Pressure and electron signal follow a similar evolution.

Fig. 7, which validates the initial assumption in Eq. (4), and supports the idea of electron clouds as the driving mechanism for the pressure rises in RHIC. This linear relation has been found also in other accelerators [18,19]. The black line shows the result of a linear regression applied to the red points,

$$P = A + B\langle V \rangle_\tau, \quad (13)$$

where  $A$  and  $B$  are the fitting coefficients. The independent term  $A$  is given by the static pressure and the electron detector signal baseline. It follows that the desorption

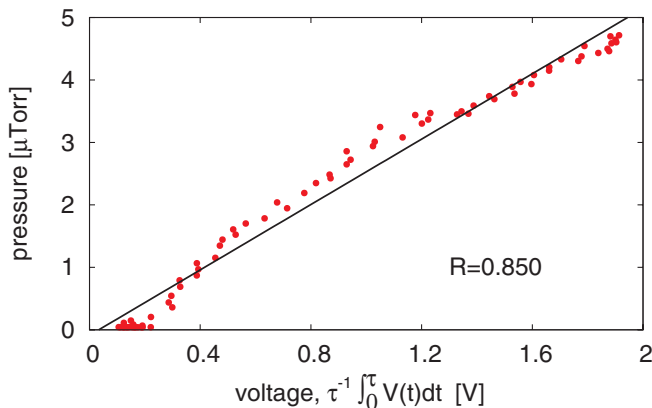


FIG. 7. (Color) Linear fit (black line) to the experimental data (red points) from Fig. 6. The fit includes the data until the beam is dumped. The linear relation between the pressure and the ED voltage  $\langle V \rangle_\tau$  is confirmed, in this case, for unbaked stainless steel surface.

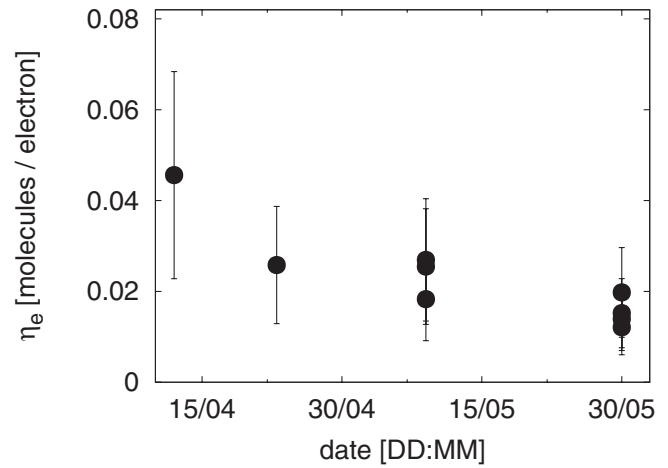


FIG. 8. Summary of all calculated desorption coefficients for the unbaked surface BO2. The error bar (50%) stems from the uncertainty in the pumping speed and vacuum pressure readings. A slight decrease of the desorption coefficient with time is noticeable due to the scrubbing effect.

coefficient,  $\eta_e$  is

$$\eta_e = B \frac{e}{kT} \frac{S}{L} \frac{ZGA_{ED}T_{eff}}{2\pi b}. \quad (14)$$

For the case in Fig. 6, the correlation coefficient is  $R = 0.850$ , the error in  $B$  is 2%, and the desorption coefficient (CO equivalent) is  $\eta_e = 0.01 \pm 0.005\%$  molecules/electron. The error in  $\eta_e$  stems from the uncertainty in the pressure reading and pumping speed values [9]. The injection shown in Figs. 6 and 7 took place at the end of the run, after the surface was conditioned by electron bombardment for several weeks during operation.

This analysis is performed for all the fills during 2003 that produced electron detector signals above the noise level. Figure 8 shows the evolution of the calculated desorption coefficient until the end of the run. As expected, this coefficient decreases with time due to the bombardment dose. In about 6 weeks,  $\eta_e$  decreased by almost a factor of 5. An estimate of the total bombardment dose is difficult. The signal-to-noise ratio of the electron detector does not allow electron signals to be obtained under about 0.15 V, even though pressure rises are observed.

#### IV. ELECTRON INDUCED DESORPTION OF BAKED STAINLESS STEEL

An example of an electron cloud, and its correlation with the pressure in IR12 is shown in Fig. 9. Once injection into the blue ring has finished (blue line, bottom plot), the electron cloud is triggered after approximately 36 bunches are injected in the yellow ring (red line, bottom plot), and both the pressure (red trace, top plot) and the electron signal (black points, top plot) start increasing at the same rate. Note the “swing” in both the electron signal and the

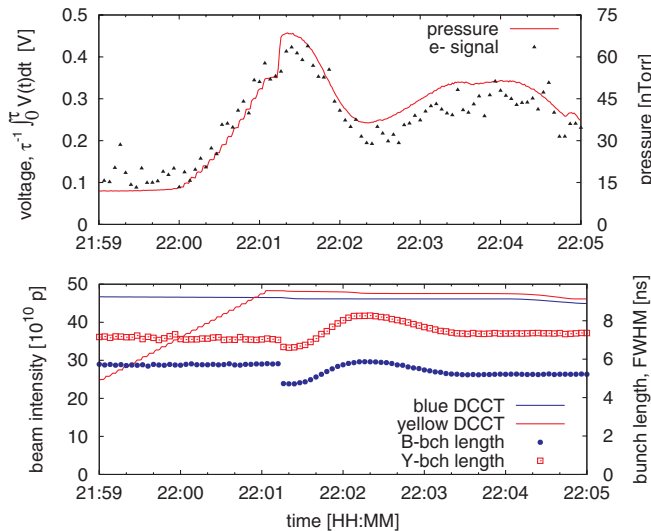


FIG. 9. (Color) Dynamic pressure evolution and electron signal (top plot), as the blue beam is being injected and ramped (bottom plot). At the beginning of the energy ramp (22:01:20) the rf voltage is raised leading to shorter bunches.

pressure evolution (top plot), as the bunch length (denoted with blue and red squares for the blue and yellow beam, respectively) swings during the ramp (bottom plot). Shorter bunches produce electrons with larger striking energies at the wall, and if this energy is below the energy at which the secondary emission yield has its maximum, this translates into a larger number of secondaries, or in other words, a larger flux into the wall. Again, the correlation between pressure and electron detection is confirmed when plotting the electron detector voltage versus the pressure (see Fig. 10). For the particular case in Fig. 10,

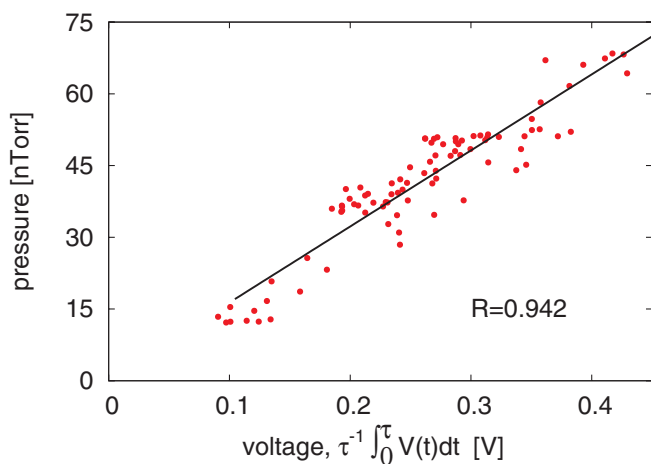


FIG. 10. (Color) Linear fit (black line) to the experimental points (red dots) shown in Fig. 7. As for the unbaked surface, a linear relation between the electron signal and the pressure is confirmed.

the calculated desorption coefficient is  $\eta_e = 0.004 \pm 0.002\%$ ,  $R = 0.942$ , and the error in B is 3.7%.

Figure 11 shows the analysis for all the fills that produced electron signals in IR12 during 2004. Note that no scrubbing effect is seen. It is possible that the chamber is sufficiently conditioned by baking, or that the low energy electrons do not lead to observable conditioning. This could also be due to the presence of the hydrogen jet installed to measure beam polarization. The jet injects an extra gas load, and runs almost continuously to measure the beam polarization [20]. If one understands the scrubbing as a “cleaning” effect, the injection of gas can cancel this effect. The average and standard deviation of the measurement shown in Fig. 11 are  $\eta_e = 0.004 \pm 0.001$  molecules/electron. This is about an order of magnitude less than the desorption coefficient of the unbaked and unscrubbed surface.

A direct comparison between the desorption coefficient obtained from this analysis and literature values is difficult because it involves different surfaces, different electron energy ranges, bombardment doses at different energies, etc. Reference [11] reports on the stainless steel desorption coefficient and its variation with the temperature, fixing the incident electron energy at 300 eV. A fiducial value for CO is  $\eta_e = 0.01$  molecules/electron. For the “as received” OFHC Copper reported in Ref. [12], the CO desorption coefficient decreases from  $\eta_e = 0.05$  molecules/electron for 300 eV electron energies to  $\eta_e = 0.005$  molecules/electron at 20 eV, and Ref. [21] shows that this value can decrease by 3 orders of magnitude after a proper bombardment dose. All in all, we conclude that results for both baked and unbaked surfaces agree in the order of magnitude with laboratory measurements [11,12,21].

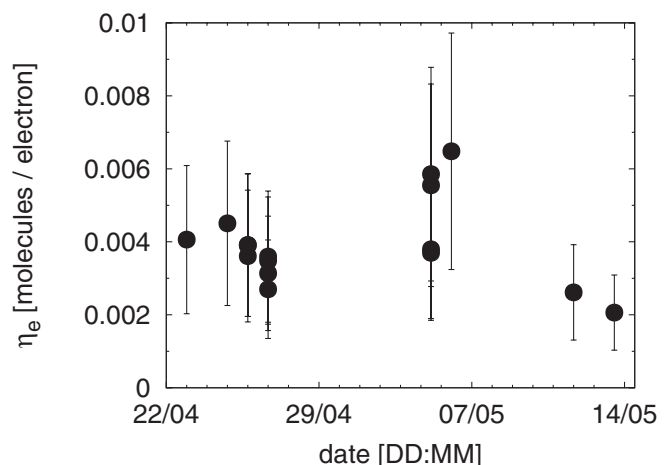


FIG. 11. Summary of all calculated desorption coefficients for the baked stainless steel surface at IR12 during 2004. The error bar is about 50% of the calculated value due to uncertainty in the pumping speed and vacuum pressure readings. The average and rms are  $0.004 \pm 0.001$  molecules/electron.

## V. ELECTRON ENERGY DURING MULTIPACTING CONDITIONS

### A. Experimental results using the electron detector

The desorption coefficient strongly depends on the energy of the electron when it strikes the beam-pipe wall. The energy spectrum of the cloud electrons was measured during a fill for the unbaked surface (see Fig. 4). The measurement was taken during a beam experiment with bunch intensities ranging from  $N_b = 1.4$  to almost  $2 \times 10^{11}$  protons, about twice as large as the operational bunch intensities at the time.

Several energy sweeps were carried out using the instrumentation shown in Fig. 2. These sweeps consist in *ramping* grid 1 from 0 to  $-500$  V (with  $-500$  V, no electron flux is detected). The peak ED signal is proportional to the number of electrons whose energy is larger than  $|eV_{\text{grid}}|$ . In this way an integrated spectrum is obtained. We use the *MADC* peak electron signals because its sampling rate (1 Hz) is faster than the scope mode (0.25 Hz), and it is synchronized to the power supply in grid 1. The right-hand side plot in Fig. 12 shows the absolute peak electron signal as a function of grid 1 voltage ( $|V_{\text{grid}}|$ ) for two different sweeps (curves with red dots and black triangles). As expected, an increase in the grid voltage reduces the peak electron signal. The signal rapidly decreases between 0 and almost 100 V, and it is close to the noise level when the grid voltage (in absolute value) is larger than 300 V.

The derivatives of these curves provide the flux at the particular energy  $|eV_{\text{grid}}|$ . The normalized electron flux at a given energy (or grid voltage) is calculated using the central differences method, where the bins with index  $i \pm 2$  are used to avoid noise oscillations:

$$\frac{1}{N_e} \frac{dN_e(E_i)}{dE} = \frac{1}{V_0} \frac{V_{i+2} - V_{i-2}}{E_{i+2} - E_{i-2}}, \quad (15)$$

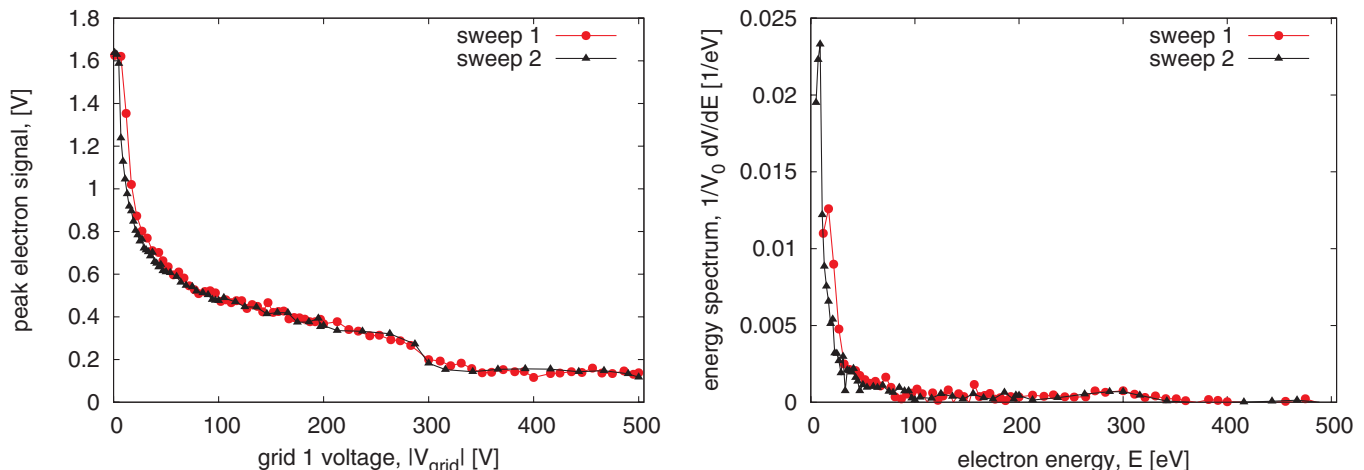


FIG. 12. (Color) Two measured integrated energy spectrum (left-hand side plot), and the derived electron distribution (right-hand side plot) for energies between 0 and 500 eV. The amplitude of the noise oscillations is about 0.15 V.

where  $E_i = |eV_{\text{grid}}|$ , and  $V_0$  is the electron signal for a null grid 1 bias voltage,  $V_{\text{grid}} = 0$  V. Note that a possible attenuation in the *MADC* process is not important because Eq. (15) only accounts for relative values. The right-hand side plot in Fig. 12 shows the normalized electron flux calculated from the integrated spectra (left-hand side plot) using Eq. (15). The two main features are the large peak of low energy electrons ( $\approx 10$  eV), and a spectrum extending to about 300 eV. Since the noise in the ED is around 0.15 V, the upper energy limit for the energy spectrum cannot be concluded definitely.

### B. Simulation results using CSEC

Table II lists the main beam parameters with which the energy spectrum was taken. The electron cloud behavior has been reproduced using the code CSEC [6,7] to compare the electron energy spectrum obtained in measurement and simulation. A key ingredient for all simulations is the secondary electron yield (SEY) as a function of the primary energy. In this case, CSEC follows the parametrization in Ref. [22], whose main parameters are listed in the second part of Table II. These parameters have not been measured *in situ*, thus their values are unknown. We use stainless steel values found in the literature [22]. For illustrative purposes, we simulate the same case with two different values of the maximum SEY:  $\delta_{\text{max}} = 1.65$  (left plot in Fig. 13), and  $\delta_{\text{max}} = 2.05$  (right plot in Fig. 13), and in both cases, we scan the bunch intensities from  $N_b = 1.4$  to  $2 \times 10^{11}$  protons, in steps of  $0.2 \times 10^{11}$  protons. For an easy comparison, we add in both cases the two experimental results in from Fig. 12.

It is remarkable that for all tested bunch intensity  $N_b$ , the energy spectrum shape is approximately the same for both  $\delta_{\text{max}} = 1.65$  or  $\delta_{\text{max}} = 2.05$  (especially for energies larger than  $\approx 100$  eV). This is an indication that the energy spectrum in RHIC mainly depends on the beam param-

TABLE II. List of beam parameters during the energy spectrum measurement. The second part of the Table shows the SEY parameters used in the CSEC simulations, whose meaning are found in Ref. [6,22].

Parameter	Symbol	Unit	Value
Number of bunches	$n$	...	60
Average bunch population	$N_b$	protons	$1.6 \times 10^{11}$
Bunch spacing	$s_b$	ns	107
Full bunch length	$4\sigma_z$	ns	15
Rms bunch radius	$\sigma_r$	mm	2.0
Chamber radius	$b$	mm	60
Revolution time	$\tau$	$\mu s$	12.8
Maximum SEY	$\delta_{\max}$	...	1.65 and 2.05
Reflection probability for $E \rightarrow 0$	$\delta_0$	...	0.6
Reflection probability for $E \rightarrow \infty$	$\delta_\infty$	...	0.15
Energy at maximum SEY	$E_{\max}$	eV	305
Reflection energy	$E_r$	eV	60
Energy of secondary emitted electrons	$E_{\text{sec}}$	eV	8.9
Distribution width of secondary electrons	$\sigma_{\text{sec}}$	eV	5
SEY exponent	$s$	...	1.83

ters. The simulated energy spectrum is not far off from the experimental one. The comparison between experimental and simulated electron energy spectra can be summarized as follows: :

(i) Both the experimental and the simulated results show a large peak of low energy electrons. Nonetheless, while the experimental spectrum peaks at about 10 eV, the simulated one peaks at 0 eV. For low energies the transparency decreases (see Fig. 15). Thus, although electrons below  $\approx 5$  eV hit the inner part of the chamber surface, their experimental detection is difficult.

(ii) For bunch intensities between  $1.6$  and  $2.0 \times 10^{11}$  protons, the spectra in Fig. 13 extend to about 300 eV, as do the experimental spectra. The reliability of the experimen-

tal results for high energy electrons (about  $\approx 300$  eV) is low because the flux at these energies is similar to the noise level.

No electron energy spectrum could be taken using the instrumentation in the baked surface due to technical difficulties with the power supply of the grid voltage. Measured and simulated in electron spectra, shown in Fig. 13, explain the slow RHIC surface conditioning, since energetic electrons are more efficient at scrubbing the surface than low energy electrons. This is valid for both for the electron desorption coefficient  $\eta_e$ , and SEY [23,24]. Usually, for the same beam conditions the electron fluxes in baked surfaces are smaller, and thus, a slow conditioning of its surface (as seen in Fig. 11) is not surprising.

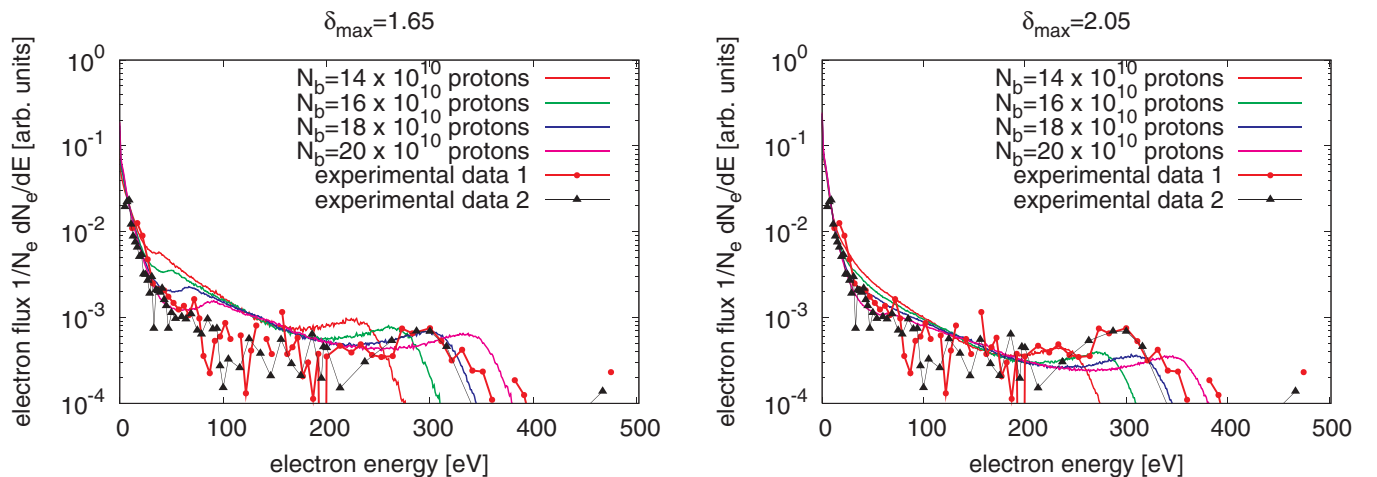


FIG. 13. (Color) Energy spectrum for  $\delta_{\max} = 1.65$  (right)  $\delta_{\max} = 2.05$  (left) and different bunch intensities. The spectrum shape is not significantly affected by the  $\delta_{\max}$ , but it depends on the beam parameters (bunch intensity, length, etc.).

## VI. SUMMARY

A linear relation between the pressure and the electron flux into the wall due to an electron cloud has been observed. The electron desorption coefficient  $\eta_e$  is inferred from the analysis of the experimental data. For unbaked stainless steel and assuming CO as the only desorbed gas, this value is about 0.05 at the beginning of the run, and decreases to 0.01 after 6 weeks of machine operation due to scrubbing. For baked stainless steel, this value is around 0.005, and no scrubbing effect is noticeable. For unbaked stainless steel, a measure of the energy spectrum shows a large peak around 10 eV. The spectrum extends to at least 300 eV. This is in generally good agreement with the spectrum obtained using CSEC simulations.

## ACKNOWLEDGMENTS

We are indebted to M. Blaskiewicz for pointing out subtle features of the electron detector signals, and to H. C. Hseuh, who patiently provided all vacuum related parameters. We are also thankful to P. He, H. Huang, D. Gassner, J. Gullotta, R. C. Lee, L. Smart, V. Ptitsyn, P. Thieberger, and S. Y. Zhang for discussions and help. Many thanks to E. Mustafin (GSI), V. Baglin, and J.-M. Laurent (CERN) for helpful discussions. Work was supported by U.S. DOE under Contract No. DE-AC02-98CH1-10886.

## APPENDIX: CALIBRATION OF THE ELECTRON DETECTOR

Two calibrations are required for inferring the electron flux at the RHIC beam pipe from a given electron detector voltage. First, a frequency calibration ensures that the signal as a function of the frequency is not attenuated due to the system electronics, cable length, etc., Second, a flux calibrations provides the relation between the flux received at the collector and the flux at the beam-pipe wall; that is to say, it evaluates the electrons lost between the grids and the collector plate (see Fig. 2).

### 1. Frequency calibration

Using a signal generator, sine-wave signals of different frequencies were introduced at the electron detector (inside the tunnel), and measured at the scope inside the service building (see Fig. 2). The total cable length is approximately 150 m. From the measured ratio between the signal generator and the scope voltage values, one can establish the frequency calibration shown in Fig. 14. The frequency range of interest is between the revolution frequency (78 kHz) and the bunch spacing frequency (10 MHz). Note that the attenuation in this range is reasonably flat and around 1 dB. The 3 dB frequency limit bandwidth is at 50 MHz.

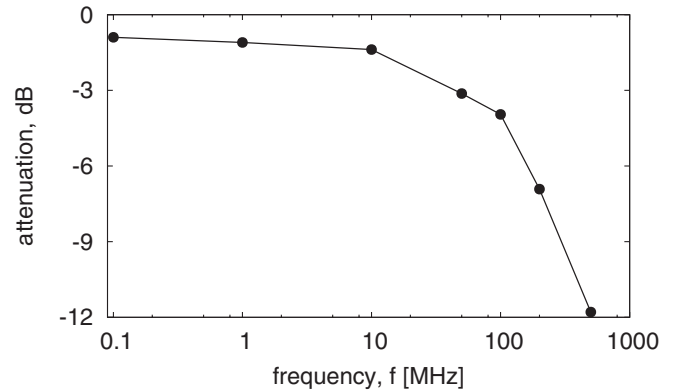


FIG. 14. Bandwidth calibration of the electron detector. The signal is reasonable flat and attenuated by less than 3 dB up to about 50 MHz.

### 2. Flux calibration

The amount of electrons lost between the grids and the collector is calibrated using the test chamber setup shown in Ref. [25]. By means of an electron gun, monoenergetic electron jets are sent at different energies to the electron detector. The ratio between the flux at the gun and the flux collected in the electron detector provides the effective transparency. The effective transparency as a function of the grid voltage is

$$T_{\text{eff}}(V_{\text{grid}}) = T_{\text{eff}}^E \theta(E - |eV_{\text{grid}}|), \quad (\text{A1})$$

where  $\theta$  is the “step” Heaviside function, and  $E$  is the energy of the monoenergetic flux (whose transparency  $T_{\text{eff}}^E$  is being calibrated). The energy spectrum for each of these monoenergetic beams is given by the derivative of Eq. (A1), that is, a Dirac’s delta function. Figure 15 shows the results for electron energies  $E = 5, 20, 50, 100,$  and  $500$  eV. By varying the filter grid bias,  $V_{\text{grid}}$ , the electron

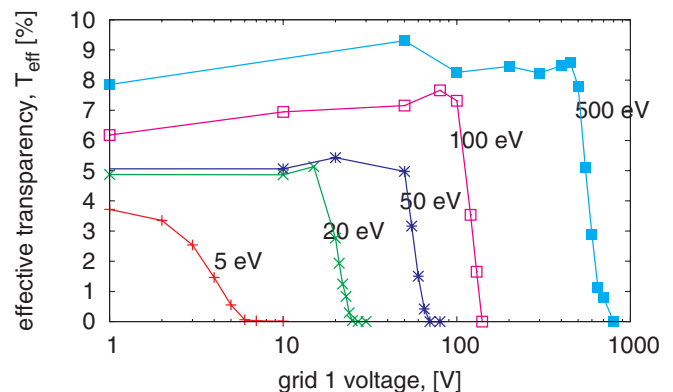


FIG. 15. (Color) Effective transparency of the electron detector. The flux coming from the electron gun vanishes when the grid voltage equals the energy of the incoming electron jet. The transparency for electrons with an energy of 500 eV is twice as large as the transparency for electrons with 5 eV.

flux is reasonably flat until  $E \approx |eV_{\text{grid}}|$ , where it becomes null. One can see that the output is reasonably flat until the filter bias reaches approximately the energy of the electron beam, that is, when  $|eV_{\text{filter}}| \approx E$ . More details about the calibration process can be found in Refs. [10,25].

Since the electron clouds in RHIC contain mainly low energy electrons (see Fig. 12 a good average value for the effective transparency is  $T_{\text{eff}} = 5\%$ ).

- 
- [1] W. Fischer, M. Bai, J.M. Brennan, M. Blaskiewicz, P. Cameron, H. C. Hseuh, H. Huang, W. MacKay, T. Roser, T. Satogata, L. A. Smart, D. Trbojevic, and S. Y. Zhang, in *Proceedings of the 8th European Particle Accelerator Conference, Paris, 2002* (EPS-IGA and CERN, Geneva, 2002).
- [2] S. Y. Zhang, BNL Report No. C-A/AP/67, 2002.
- [3] H. Hseuh, L. Smart, and S. Y. Zhang, in *Proceedings of the 8th European Particle Accelerator Conference, Paris, 2002* (Ref. [1]).
- [4] W. Fischer, M. Blaskiewicz, P. He, H. Huang, H. C. Hseuh, U. Iriso, G. Rumolo, L. Smart, D. Trbojevic, and S. Y. Zhang, in *Proceedings of ELOUD'04, Napa Valley, 2004* (CERN, Geneva, 2005).
- [5] *Proceedings of CERN Accelerator School on Vacuum Technology, Snekersten, Denmark*, edited by S. Turner (CERN, Geneva, 1999).
- [6] W. Fischer, M. Blaskiewicz, M. Brennan, and T. Satogata, *Phys. Rev. ST Accel. Beams* **5**, 124401 (2002).
- [7] M. Blaskiewicz, M. Furman, M. Pivi, and R. Macek., *Phys. Rev. ST Accel. Beams* **6**, 014203 (2003).
- [8] G. Stupakov, CERN-LHC-Project-Report-141, 1997.
- [9] H. C. Hseuh (private communications).
- [10] U. Iriso, A. K. Drees, W. Fischer, D. Gassner, O. Gould, J. Gullotta, P. He, H. C. Hseuh, R. Lee, V. Ponnaiyan, L. Smart, D. Trbojevic, and S. Y. Zhang, CAD/AP/129, 2003.
- [11] J. Gómez-Goni and A.G. Mathewson, *J. Vac. Sci. Technol. A* **15**, 3093 (1997).
- [12] F. Billard, N. Hilleret, and G. Vorlaufer, CERN LHC/VAC/FB/NH/GV00-32, 2000.
- [13] R. Macek *et al.*, in *Proceedings of the Workshop on Two Stream Instabilities, KEK, Tsukuba, Japan, 2001*, <http://conference.kek.jp/two-stream/>.
- [14] R.A. Rosenberg and K.C. Harkay, *Nucl. Instrum. Methods Phys. Res., Sect. A* **453**, 507 (2000).
- [15] U. Iriso and J-M. Laurent, CERN Vacuum Technical Notes LHC-VAC, TN03-05, 2003.
- [16] Z. Y. Guo *et al.*, in *Proceedings of the Particle Accelerator Conference, Chicago, 2001* (IEEE, Piscataway, NJ, 2001).
- [17] U. Iriso, Ph.D. thesis, Universitat de Barcelona, 2005 (to be published).
- [18] K. Kanazawa and H. Hisamatsu, Presentation at BNL, 2004.
- [19] Y. Suetsugu, in *Proceedings of the Particle Accelerator Conference, Chicago, 2001* (Ref. [16]).
- [20] A. Zelenski, A. Bravar, D. Graham, W. Haerberli, S. Kokhanovski, Y. Makdisi, G. Mahler, A. Nass, J. Ritter, T. Wise, and V. Zubets, *Nucl. Instrum. Methods Phys. Res., Sect. A* **536**, 248 (2005).
- [21] N. Hilleret, B. Henrist, C. Scheuerlein, M. Taborelli, G. Vorlaufer. The Variation of the Secondary Electron Yield and of the Desorption Yield of Copper under Electron Bombardment: Origin and Impact on the Conditioning of LHC, in *Proceedings of the 8th European Particle Accelerator Conference, Paris, 2002* (Ref. [1]), p. 2553.
- [22] M. A. Furman and M. Pivi, *Phys. Rev. ST Accel. Beams* **5**, 124404 (2002).
- [23] V. Baglin, I.R. Collins, O. Gröbner, C. Grünhael, B. Henrist, N. Hilleret, and B. Jenninger, in *Proceedings of the LHC Workshop—11th Chamonix Workshop: LHC* (CERN, Geneva, 2001).
- [24] F. Billard, N. Hilleret, and G. Vorlaufer., CERN Technical Report No. LHC/VAC/FB/NH/GV/00-32, 2000.
- [25] P. He, H. C. Hseuh, D. Gassner, J. Gullotta, D. Trbojevic, and S. Y. Zhang, in *Proceedings of the Particle Accelerator Conference, Portland, OR, 2003* (IEEE, Piscataway, NJ, 2003).